

Loading Path and Control Mode Effects During Thermomechanical Cycling of Polycrystalline Shape Memory NiTi

D. E. Nicholson^{1,4} · O. Benafan² · S. A. Padula II² · B. Clausen³ · R. Vaidyanathan¹

Published online: 23 January 2018
© ASM International 2018

Abstract Loading path dependencies and control mode effects in polycrystalline shape memory NiTi were investigated using in situ neutron and synchrotron X-ray diffraction performed during mechanical cycling and thermal cycling at constant strain. Strain-controlled, isothermal, reverse loading (to $\pm 4\%$) and stress-controlled, isothermal, cyclic loading (to ± 400 MPa for up to ten cycles) at room temperature demonstrated that the preferred martensite variants selected correlated directly with the macroscopic uniaxial strain and did not correlate with the compressive or tensile state of stress. During cyclic loading (up to ten cycles), no significant cycle-to-cycle evolution of the variant microstructure corresponding to a given strain was observed, despite changes in the slope of the stress–strain response with each cycle. Additionally, thermal cycling (to above and below the phase transformation) under constant strain (up to 2% tensile strain) showed that the martensite variant microstructure correlated directly with strain and did not evolve following thermal cycling, despite relaxation of stress in both martensite and austenite phases. Results are presented in

the context of variant reorientation and detwinning processes in martensitic NiTi, the fundamental thermoelastic nature of such processes and the ability of the variant microstructure to accommodate irreversible deformation processes.

Keywords Twinning · Mechanical behavior · Martensite

Introduction

Polycrystalline NiTi shape memory alloys (SMAs) have the ability to recover their pre-deformed shape against external loads as a result of being heated through a reversible solid-state phase transformation from a lower-symmetry B19' martensite phase to a higher-symmetry B2 austenite phase [1–3]. In the process of returning to the pre-deformed shape, SMAs can recover a considerable amount of deformation (e.g., up to 8% strain) against large stresses (e.g., up to 500 MPa). This ability to do work while transforming from one phase to another enables their use as high-force actuators with both sensory and actuation functions [4]. To facilitate the implementation of SMA actuators in applications, a better understanding of the relationship between the isothermal (mechanical deformation at constant temperature), isostrain (thermal cycling under constant strain), and isobaric (thermal cycling under constant stress) responses and the effects of the control mode adopted (stress- or strain-controlled loading) is required [5]. Recent examples of improving the understanding of the relationship between such thermomechanical loading paths include investigations which highlighted the ability to take different paths by either isothermal or isobaric loading yet still obtain a similar microstructure and actuation response [6]. This ability to obtain similar

✉ R. Vaidyanathan
raj@ucf.edu

¹ Advanced Materials Processing and Analysis Center (AMPAC), Department of Mechanical and Aerospace Engineering, Department of Materials Science and Engineering, University of Central Florida, Orlando, FL 32816, USA

² NASA Glenn Research Center, Cleveland, OH 44135, USA

³ MST-8, Los Alamos National Laboratory, P.O. Box 1663, MS H805, Los Alamos, NM 87545, USA

⁴ Present Address: The Boeing Company, 6300 James S. McDonnell Blvd., Berkeley, MO 63134, USA

microstructures by various loading paths could be utilized for designing loading paths which minimize the training and processing required to obtain an optimized actuation response [7, 8].

During isothermal loading of martensitic NiTi, deformation mechanisms including elasticity, martensite variant reorientation or coalescence and detwinning, and dislocation-based plasticity have been shown to be active; however, the ability to decouple the contribution of each mechanism to the overall macroscopic response remains a challenge [9]. Progress in decoupling the contributions of each mechanism included the determination of the anisotropic elastic stiffness constants of B19' NiTi using ab initio calculations [10] and in situ neutron diffraction experiments [11]. Initial tensile loading (up to 1%) is primarily attributed to elastic deformation with limited variant reorientation and detwinning. From neutron diffraction experiments, it was shown that detwinning and variant reorientation processes can occur at strains less than 0.2%. As tensile strain is increased (to between ~ 1 and $\sim 6\%$ strain), detwinning and variant reorientation becomes the dominant deformation mechanism [11]. Inverse pole figures (IPFs) have previously been used to correlate changes in texture to preferred selection of martensite variants in Refs. [6, 8, 9, 11, 12]. Preferred tensile and compressive variant selection was commonly observed (in IPFs, w.r.t. the loading direction) as an increase in multiples of random distribution (MRD) near the $(010)_M$ and $(111)_M$ crystallographic poles, respectively. Transmission electron microscopy (TEM) investigations showed that $[011]_M$ type II and $(1\bar{1}1)_M$ type I twinning are the dominant twinning modes in this region [13–15]. In these regions of loading, dislocations in martensite twin plates [15] and both junction plane areas [16] have been observed. At tensile strains greater than $\sim 6\%$, an increase of the slope of the stress–strain response occurs as a result of $(001)_M$ and $(20\bar{1})_M$ deformation twins becoming active and increasing dislocation density [17]. As tensile strain continues to increase in tension (to between 6 and $\sim 12\%$ strain), an increase in MRD near the $(\bar{1}50)_M$ and $(010)_M$ poles occurs, as observed in IPFs in Ref. [8]. At strains greater than $\sim 12\%$, MRD near the $(\bar{1}50)_M$ and $(010)_M$ poles decreases and increases near the $(230)_M$ pole, possibly as a result of $(001)_M$ and $(20\bar{1})_M$ deformation twins and dislocation-based plasticity becoming the dominant deformation mechanisms.

Previous investigations have included tension–compression cyclic isothermal loading (up to $\pm 4\%$ strain for 50 cycles) under strain control [15, 16]. Utilizing TEM, it was shown that $[011]_M$ type II twinning was the primary twinning system prior to cycling. Following cycling, $(11\bar{1})_M$ type I twinning was most frequently observed after

cycling and was attributed to reoriented martensite variants. It was also reported that after cycling a high density of dislocations developed in both junction plane areas and within the martensite twins. It was concluded that these aforementioned deformation mechanisms contributed to changes in the slope of the stress–strain response with cycling.

Thermal cycling at constant strain of SMAs can be used to limit strain to increase the engineering life of an SMA actuator [7] in applications requiring large forces in compact spaces [18], e.g., a static rock splitter for planetary exploration [19]. Additionally, the shape-setting process [20] is typically performed by thermally cycling to above and below the phase transformation under constant strain. During in situ neutron diffraction shape-setting experiments of polycrystalline NiTi (49.9 at.% Ni), tensile strain (up to 7.3%) was held constant while the specimen was thermally cycled (up to 450 °C) [20]. While heating, blocking stresses were generated and reached a maximum of 400 MPa at 200 °C and subsequently relaxed to near zero as heating continued to 450 °C. At room temperature following the shape-set, the specimen showed zero macroscopic stress and a self-accommodated microstructure (observed in IPFs). Constant strain thermal cycling (between 30 and 300 °C) in $\text{Ni}_{50.3}\text{Ti}_{29.7}\text{Hf}_{20}$ resulted in blocking stresses up to 1.5 GPa in the first cycle which decayed and stabilized to 1.1 GPa following subsequent cycles (up to 20) [18].

The objective of the current study seeks to provide microstructural and macroscopic insight into loading path and control mode effects in shape memory NiTi. This is achieved using in situ neutron and synchrotron X-ray diffraction wherein information representative of the bulk, i.e., phase fraction and texture evolution, was followed during stress- and strain-controlled, isothermal, reverse loading and constant strain, thermal cycling of near-equiatomic polycrystalline NiTi. Results are presented in context of variant reorientation and detwinning processes in martensitic NiTi and the fundamental thermoelastic nature of such processes. Discussion of the results is extended to include isobaric loading and inferences are made regarding the behavior of shape memory NiTi under general loading conditions.

Experimental Procedures

Material

The material used in this work was a binary NiTi alloy (nominal composition 49.9 at.% Ni), produced by Special Metals (now SAES Smart Materials, New Hartford, NY). This alloy is part of a large material lot that has been

extensively studied elsewhere [6, 8, 11, 20–23, 35, 36]. Ten-millimeter rods were produced in the hot-rolled/hot-drawn and hot-straightened condition. The martensite finish (M_f), martensite start (M_s), austenite start (A_s), and austenite finish (A_f) transformation temperatures were determined by differential scanning calorimetry to be 46, 71, 86, and 102 ± 2 °C, respectively.

In Situ Neutron Diffraction

The following experiments were performed in situ in “time-of-flight” mode using the Spectrometer for Materials Research at Temperature and Stress (SMARTS) at Los Alamos National Laboratory (LANL). The experimental setup at SMARTS is only summarized here and additional details can be found in Ref. [24]. Figure 1a shows the

detector coverage at SMARTS that was utilized in this work. Figure 1a illustrates the physical location of the detector banks w.r.t. the incident beam and specimen. The loading axis forms 45° angle with the incident neutron beam. Two detector banks are positioned at opposing 90° angles relative to the beam which allows for reflections from lattices planes parallel and perpendicular (indicated by 1 and 2, respectively, in Fig. 1) to the loading axis to be captured. A third detector bank (indicated by 3 in Fig. 1) was positioned directly below the incident beam in a backscattering geometry with a scattering angle of 155° . Figure 1b shows the detector coverage of the three banks, projected onto a pole figure. Results presented henceforth will correspond to reflections from lattices planes perpendicular to the loading axis unless otherwise stated.

Cylindrical dog-bone samples were machined to 5.08 mm gauge diameter and 15.24 mm gauge length with threaded ends. Prior to all experiments, two no-load, thermal cycles between room temperature and 200 °C were performed after installation into the load frame in order to ensure an initial self-accommodated microstructure. Compression–tension (i.e., compression followed by tension) and tension–compression (i.e., tension followed by compression), reverse, cyclic isothermal loading was performed in strain control to $\pm 4\%$ for ten cycles at room temperature, on two different specimens. Neutron diffraction spectra were acquired at 2% strain increments on the first, second, and tenth cycle. Tension–compression, reverse, cyclic, isothermal loading was performed in stress control to ± 400 MPa for ten cycles at room temperature, on a third specimen. Neutron diffraction spectra were acquired at ± 400 MPa stress increments on the first, second, fifth, and tenth cycle.

Thermal cycling at constant strain was performed on two specimens at 1 and 2% tensile strain, respectively. The specimens were loaded to their respective strains at room temperature in strain control and then the strain was held constant, while the specimen was thermally cycled between 40 °C (lower cycle temperature LCT) and 165 °C (upper cycle temperature UCT) for ten cycles. Neutron diffraction spectra were acquired between the LCT and UCT on the first, second, fifth, and tenth cycle. To ensure adequate statistics for analysis, a hold time of 30 min was used to acquire each spectrum. Extensometry (10 mm gauge length and strain resolution of 5×10^{-5}) was used to report macroscopic strain measurements. During strain and stress-controlled experiments, a strain rate of 10^{-4} s $^{-1}$ and stress rate of 40 MPa/min, respectively, was maintained.

Rietveld refinement [25] implemented by General Structure Analysis System (GSAS) [26] was used to analyze all neutron diffraction spectra. Details of the implementation of this approach as it is applied to analyzing texture during heating and loading of NiTi-based alloys can

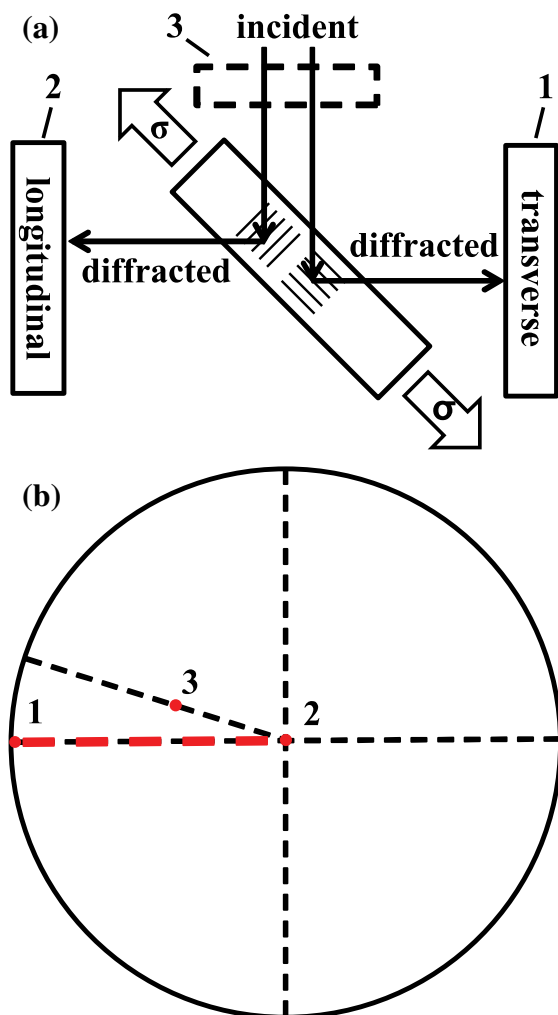


Fig. 1 Detector coverage at the SMARTS diffractometer at Los Alamos National Laboratory: **a** schematic of physical location w.r.t incident and diffracted beams, and specimen; and **b** projected onto a pole figure. All axial distribution plots generated in this paper correspond to the radial slice indicated by the dashed line between 1 and 2

be found in Refs. [11, 27, 28] among others. Inverse pole figures (IPFs) were generated from the refinements as previously outlined [29] and plotted with generic mapping tools [30]. IPFs represent the distribution of a selected direction in the specimen relative to the crystal axes in multiples of random distribution (MRD) with 1 corresponding to a random distribution. IPFs presented henceforth were generated from diffracting planes perpendicular to the loading direction, unless otherwise stated. Axial distribution plots (ADP) correspond to a radial slice (indicated by the dashed line between 1 and 2 in Fig. 1b) of the pole figure (cylindrical symmetry in the specimen was assumed) and provided a second representation of analyzing and describing texture in this work. The ADP represents MRD (y -axis) of a specified crystallographic direction oriented at an angle (φ) between the normal to the specified plane and a chosen axis in the specimen, in this case the loading direction.

In Situ Synchrotron X-ray Diffraction

Additional thermal cycling at constant strain experiments were performed using in situ synchrotron X-ray diffraction at the High Energy Materials Science (HEMS) beam line at the high-brilliance synchrotron radiation storage ring PETRA III at DESY in Hamburg, Germany. Details of the implementation of HEMS for investigations of NiTi-based alloys can be found in Ref. [31, 32] and are only summarized here. Measurements were taken with a photon energy of 100 keV ($\lambda = 0.12427 \text{ \AA}$) using a beam cross section of $500 \times 500 \mu\text{m}^2$ with a sample-to-detector distance of 1.572 m. Debye–Scherrer diffraction rings were captured using a MAR345 image plate detector (345 mm area diameter) with 100 μm pixel size. Diffraction spectra were generated by integrating diffraction rings over azimuthal intervals of 10° to ensure adequate grain statistics.

Cylindrical compression specimens, 10 mm in length and 5 mm in diameter, were loaded in displacement control using a BÄHR DIL805 dilatometer. The specimen was loaded in displacement control in compression to a strain (measured at the grips) of -0.6% , and then held at constant displacement and thermally cycled between 40 and 165 $^\circ\text{C}$ (at a heating and cooling rate of 10 $^\circ\text{C}/\text{min}$) for five cycles.

Results and Discussion

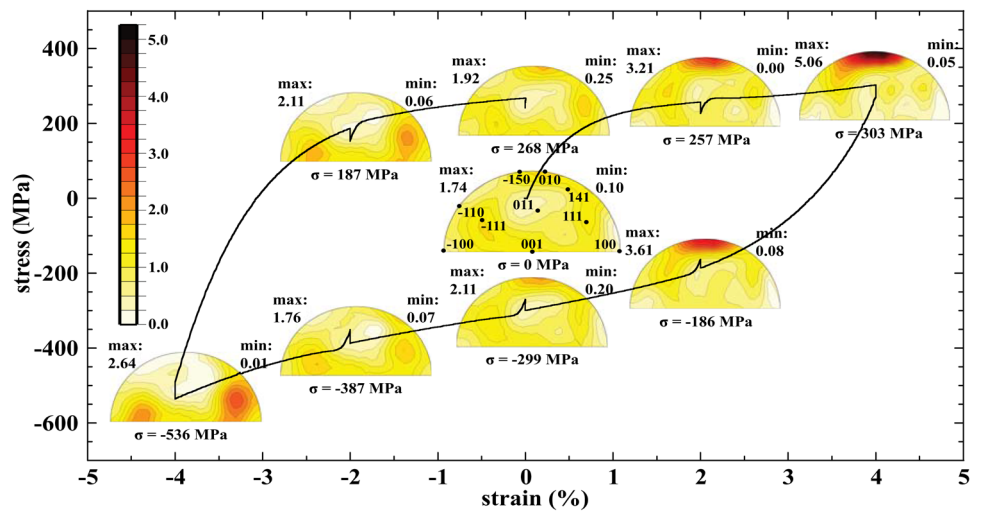
Strain-Controlled, Reverse Loading

Figure 2 shows IPFs corresponding to the first cycle of tension–compression (tension followed by compression), isothermal, strain-controlled, reverse loading of B19'

martensitic NiTi at room temperature. Initially at zero stress and strain, a near self-accommodated microstructure was established as indicated by a maximum intensity of 1.74 (this value is within ± 0.2 of previous work on this alloy [6, 11]) in the corresponding IPF. Tensile loading of the specimen to 4% strain resulted in preferred selection of variants as indicated by an increase in intensity (to a maximum of 5.06) near the 010 pole, observed in the corresponding IPF at 4%. Upon load reversal (from 4 to 0% strain), the selected variants reoriented back to that of a near self-accommodated variant microstructure as indicated by a decrease in intensity (to a maximum of 2.11) observed in the corresponding IPF at 0%. Subsequent compressive loading of the specimen to -4% strain resulted in preferred selection of other variants (those favoring compressive strains) as indicated by an increase in intensity (to a maximum of 2.64) near the 111 pole, as observed in the corresponding IPF at -4% . Upon subsequent load reversal (from -4 to 0% strain), the variants reoriented back to that of a near self-accommodated variant microstructure as indicated by a decrease in intensity (to a maximum of 1.92), again as observed in the corresponding IPF at 0%. The ability to return to a near self-accommodated texture following preferential selection of variants demonstrates the isothermal reversibility of variant reorientation and detwinning in NiTi (within the limits investigated here). Overall, at 0% strain, both, initially and following the first and second load reversals, a similar texture was observed (as indicated by maximum intensities of 1.74, 2.11 and 1.92, respectively) despite having significant differences in stress (i.e., 0, -299 and 268 MPa, respectively). This result demonstrates that martensite variant selection in NiTi correlates well with the macroscopic uniaxial strain and does not correlate with the compressive or tensile state of stress (within the limits investigated here). It is noted that there exists some remnant texture at 0% strain in both tension and compression paths (Fig. 2), but their strengths are small and overall the texture is comparable to the starting self-accommodated texture. The formation of residual texture was also noted Ref. [6] and attributed to pinning (to a limited degree) of compression and tension preferred variants by irrecoverable deformation mechanisms.

At 2% strain during loading and unloading, the maximum intensity observed in the corresponding IPFs was 3.21 and 3.61 (observed near the 010 pole), respectively. At -2% strain during loading and unloading, the maximum intensity observed in the corresponding IPFs was 1.76 and 2.11 (observed near the 111 pole), respectively. The observed hysteresis, i.e., difference in variant microstructures during unloading and loading, at an equivalent strain, can be attributed to elastic unloading of martensite and the stress required to activate variant

Fig. 2 Inverse pole figures corresponding to diffracting planes perpendicular to the loading direction during the first cycle of tension–compression (i.e., tensile followed by compressive), isothermal, strain-controlled, reverse loading of B19' martensitic NiTi at room temperature. For clarity in presentation, the scale chosen in the inverse pole figures are unique to this figure



reorientation and detwinning processes upon load reversal. Irreversible energy dissipation and irrecoverable deformation mechanisms also occur, and in some cases trap or pin some of the preferentially selected variants, hindering their reversal until adequate stress is applied.

Figure 3a shows the evolution of the stress–strain response for the first ten cycles of compression–tension (compression followed by tension) isothermal, strain-controlled, reverse loading (to ± 4% strain) of B19' martensitic NiTi at room temperature. The stress increased at the maximum compressive and tensile strains and decreased at intermediate strains with cycling. Figure 3b shows the evolution of stress at the minimum and maximum strains for the first ten cycles of isothermal, strain-controlled, reverse loading to ± 4% strain of B19' martensitic NiTi at room temperature. Note, the mean stress, defined as $\sigma_{\text{mean}} = (\sigma_{4\%} + \sigma_{-4\%})/2$, is also shown in Fig. 3b. Figure 3b shows similar changes in stress for both tension–compression and compression–tension reverse loading, indicating changes in the slope of the stress–strain curve with the overall evolution being independent of the initial loading direction. This change in the slope of the stress–strain response observed here is consistent with Refs. [15, 33, 34] wherein the observed behavior was attributed to martensite variant reorientation, twin boundary movement within martensite plates, formation of stacking faults on (001) planes, shear along (110) planes, and the accumulation of dislocations in both junction plane areas and martensite twin plate. The mean stress did not change with cycling, suggesting that the stress is changing at the maximum and minimum strains at a similar rate (with cycling) and the overall response is not shifting w.r.t. stress.

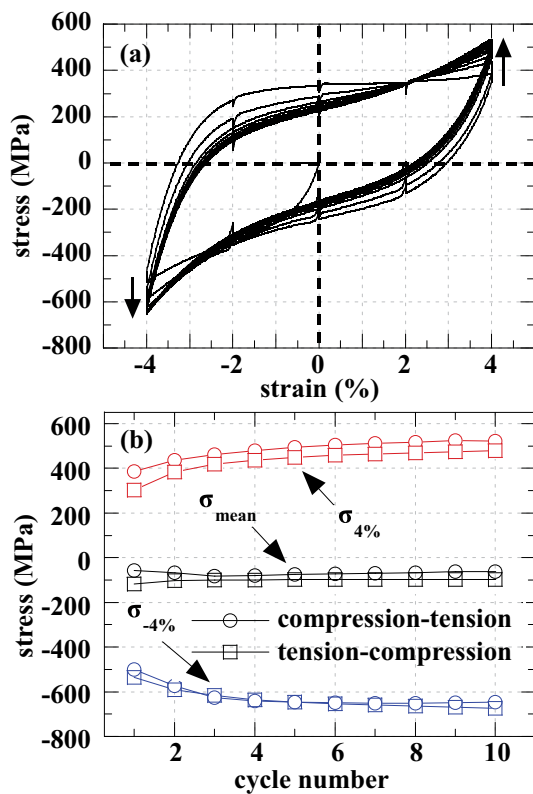


Fig. 3 Response of the first ten cycles of isothermal, strain-controlled, reverse loading of B19' martensitic NiTi at room temperature: **a** stress at ± 4% strain (indicated by $\sigma_{4\%}$ and $\sigma_{-4\%}$, respectively), for the tensile followed by compressive and compressive followed by tensile loading. The mean stress defined as $\sigma_{\text{mean}} = (\sigma_{4\%} + \sigma_{-4\%})/2$ is also shown

Figure 4 shows the IPFs corresponding to the first ten cycles of compression–tension, isothermal, strain-controlled, reverse loading at room temperature. Note that the IPFs shown in Fig. 4 correspond to the macroscopic response shown in Fig. 3a. At the following strains: 0% initial, - 4% compressive, 0% on the first load reversal (positive stress), 4% tensile, and 0% on the second load reversal (negative stress), the maximum intensities observed in the corresponding IPFs were 1.76, 3.00, 1.93,

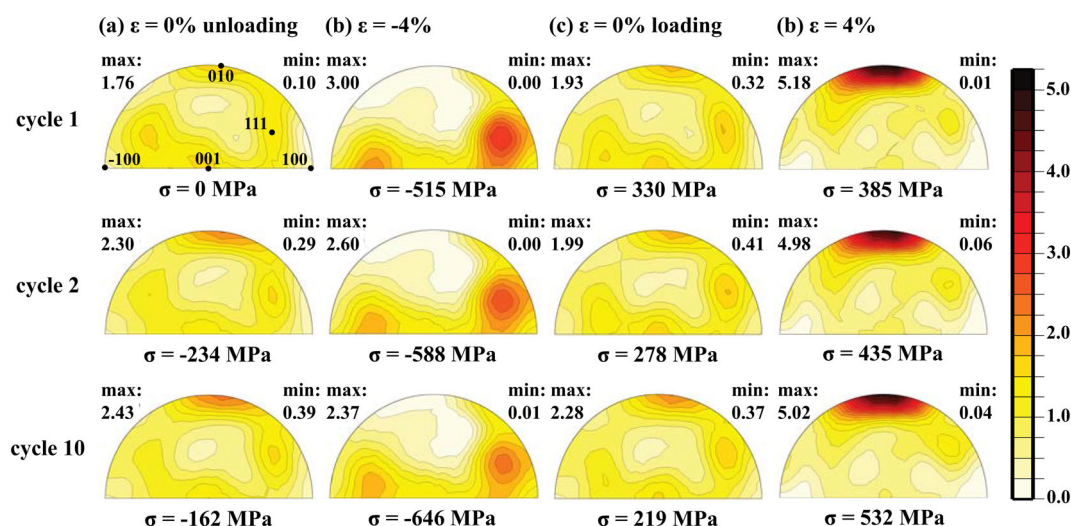


Fig. 4 Inverse pole figures corresponding to diffracting planes perpendicular to the loading direction during the first ten cycles of compressive loading followed by tensile, isothermal, strain-controlled, reverse loading of B19' martensitic NiTi at room temperature at **a** $\varepsilon = 0\%$ during unloading; **b** $\varepsilon = -4\%$; **c** $\varepsilon = 0\%$ during loading;

and **d** $\varepsilon = 4\%$ for the first, second, and tenth cycles, respectively. Note, the IPFs presented in this figure correspond to the macroscopic response shown in Fig. 3. For clarity in presentation, the scale chosen in the inverse pole figures are unique to this figure

5.18, and 2.30, respectively (comparable to 1.74, 2.64, 1.92, 5.06, and 2.11, respectively, at equivalent positions w.r.t. the tension–compression response shown in Fig. 2). This result again shows that martensite variant microstructures were equivalent for the corresponding strain whether the specimen was loaded in compression or tension and the reversibility of isothermal deformation was demonstrated when the preferentially selected variants reverted back to that of the self-accommodated variant microstructure when loading was reversed. Furthermore, these results are independent of the initial loading direction (i.e., similar in both, compression–tension or tension–compression, reverse loading paths).

At -4% strain during the first, second, and tenth cycles, the maximum intensities (near the 111 pole) observed in the corresponding IPFs were 3.00, 2.60, and 2.37, respectively, and the corresponding stresses were -515 , -588 , and -646 MPa, respectively. At $+4\%$ strain during the first, second, and tenth cycles, the maximum intensities (near the 010 pole) observed in the corresponding IPFs were 5.18, 4.98, and 5.02, respectively, and the corresponding stresses were 385, 435, and 532 MPa, respectively. At 0% strain during unloading in the first, second, and tenth cycles, the maximum intensities (near the 010 pole) observed in the corresponding IPFs were 1.76, 2.30, and 2.43, respectively, and the corresponding stresses were 0, -234 , and -162 MPa, respectively. At 0% strain during loading in the first, second, and tenth cycles, the maximum intensities (near the 010 pole) observed in the corresponding IPFs were 1.93, 1.99, and 2.28, respectively, and the corresponding stresses were 330, 278, and

219 MPa, respectively. Thus, during cyclic, strain-controlled, reverse loading the maximum intensities observed in the corresponding IPFs decreased at the maximum compressive strain, remained the same (within error) at the maximum tensile strain, and increased (during loading and unloading) at 0% strain with each cycle. Overall, the relationship between the strain and the selected variant microstructure, and the subsequent reversibility of the selected variant microstructure was unaffected. The small differences in variant microstructures during unloading and loading, at a given strain, and the residual or remnant texture observed at zero strain can be attributed to (i) elastic unloading of martensite and the stress required to activate variant reorientation and detwinning processes upon load reversal as affected by irreversible energy dissipation mechanisms (e.g., variant interface motion); and (ii) compressive strain and tensile strain preferred variants being pinned or trapped (to a limited extent) by dislocation-based plasticity (which includes mechanisms described in Ref. [15]) accumulated during cycling, slip, and/or the early onset of deformation twinning. Note, it is well known and also shown in Fig. 2 that the variants selected or preferred in tension and compression are different which give rise to the tension–compression asymmetry in the macroscopic stress–strain response.

Stress-Controlled, Reverse Loading

In order to provide additional insight into the effects of control mode on the deformation response during isothermal loading, stress-controlled, reverse loading was also

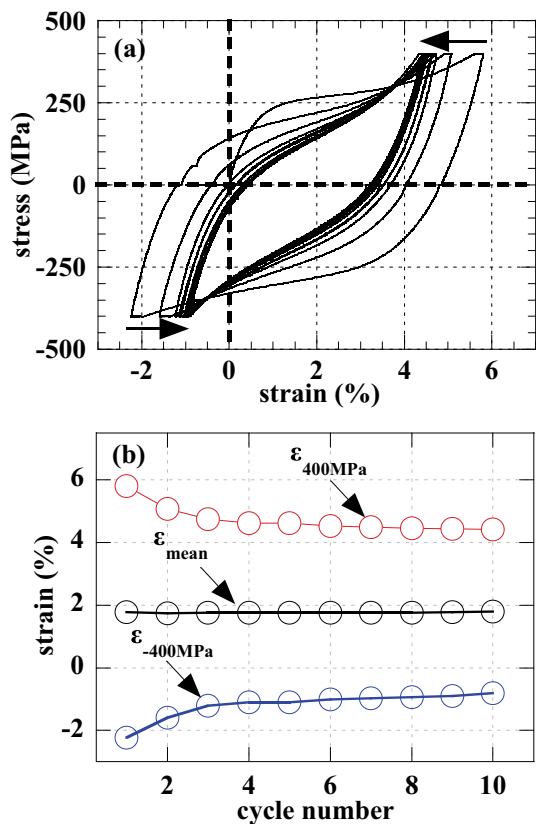


Fig. 5 Evolutionary response of the first ten cycles of isothermal tensile followed by compressive, stress-controlled, reverse loading of B19' martensitic NiTi at room temperature: **a** stress–strain response and **b** strain at ± 400 MPa (indicated by $\epsilon_{400\text{MPa}}$ and $\epsilon_{-400\text{MPa}}$, respectively). The mean strain defined as $\epsilon_{\text{mean}} = (\epsilon_{400\text{MPa}} + \epsilon_{-400\text{MPa}})/2$ is also shown

investigated. Figure 5a shows the evolution of the stress–strain response for the first ten cycles of tension–compression, isothermal, stress-controlled, reverse loading (to ± 400 MPa) of B19' martensitic NiTi at room temperature. During cyclic, stress-controlled, reverse loading, the slope of the stress–strain response increased as indicated by decreasing (absolute) strain values at maximum tensile (400 MPa) and compressive (-400 MPa) stress. To facilitate the following discussion, Fig. 5b shows the strains at the maximum tensile and compressive stress (indicated by, $\epsilon_{400\text{MPa}}$ and $\epsilon_{-400\text{MPa}}$, respectively) for each cycle. The mean strains, defined as $\epsilon_{\text{mean}} = (\epsilon_{400\text{MPa}} + \epsilon_{-400\text{MPa}})/2$, are also shown in Fig. 5b. Similar to Fig. 3, the mean strain did not change with cycling, suggesting that the strain is changing at the maximum and minimum stresses at a similar rate (with cycling) and the overall response is not shifting w.r.t. strain.

Figure 6 shows the IPFs corresponding to the first ten cycles of tension–compression, isothermal, stress-controlled (to ± 400 MPa), reverse loading of B19' martensitic NiTi at room temperature. The initial IPF (not shown)

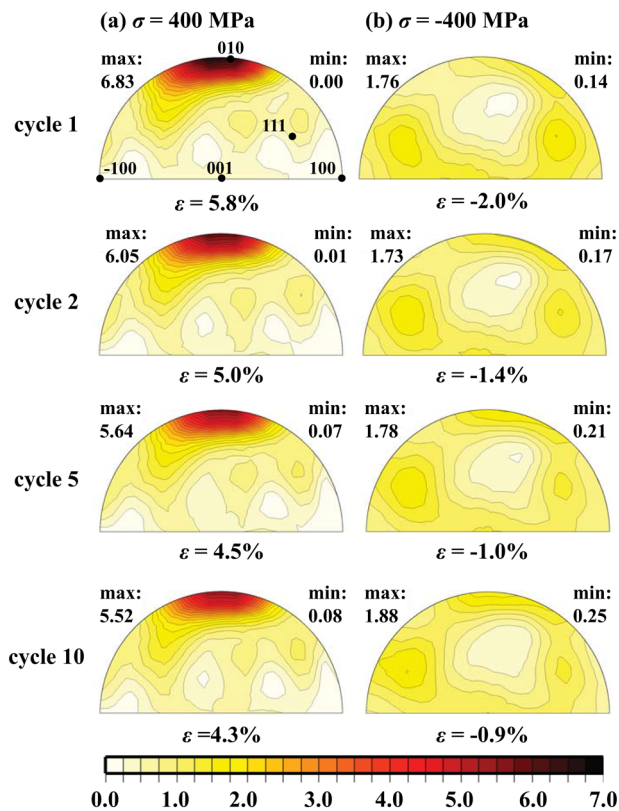


Fig. 6 Inverse pole figures corresponding to diffracting planes perpendicular to the loading direction during the first ten cycles of tensile followed by compressive, isothermal, stress-controlled, reverse loading of B19' martensitic NiTi at room temperature at **a** $\sigma = 400$ MPa and **b** $\sigma = -400$ MPa stress. Note, the IPFs presented in this figure correspond the macroscopic response shown in Fig. 5. For clarity in presentation, the scale chosen is unique to this figure

at zero stress and strain at room temperature had a maximum intensity 1.75 corresponding to that of a self-accommodated microstructure. During initial loading from 0 to 400 MPa, variants were selected as indicated by an increase in maximum intensity in the corresponding IPF (Fig. 6a, cycle one) to 6.83 (near the 010 pole) and corresponded to a strain of 5.8%. Upon reverse loading from 400 to -400 MPa, variants reverted to an almost self-accommodated microstructure as indicated by a decrease in the maximum intensity observed in the corresponding IPF (Fig. 6b, cycle one) to 1.76 and corresponded to a strain of -2.0% . The result that a near self-accommodated microstructure (as indicated by minimum texture) was observed near -2.0% strain as opposed to zero strain during unloading, after a load reversal, was also observed in the previous section (see the IPF in Fig. 2 at -2.0% strain during unloading) during strain-controlled, reverse isothermal loading. In both cases, this behavior was attributed to elastic unloading of martensite and the stress required to activate variant reorientation and detwinning processes upon load reversal as affected by irreversible

energy dissipation mechanisms (e.g., variant interface motion).

The corresponding IPFs at (a) 400 MPa and (b) – 400 MPa for the first, second, fifth, and tenth cycles are also shown in Fig. 6. At 400 MPa, the maximum intensities (near the 010 pole) observed in the corresponding IPFs were 6.88, 6.05, 5.64, and 5.52, respectively, and the equivalent strain values observed were 5.8, 5.0, 4.5, and 4.3%, respectively, for the first, second, fifth, and tenth cycles. At – 400 MPa, the maximum intensities observed in the corresponding IPFs were 1.76, 1.73, 1.78, and 1.88, respectively, and the equivalent strains values observed were – 2.0, – 1.4, – 1.0, and – 0.9%, respectively, for the first, second, fifth, and tenth cycles. During cyclic, stress-controlled, reverse loading, the maximum intensities observed in the corresponding IPFs decreased (near 010 pole) at the maximum tensile stress (400 MPa) and remained the same (within error) at the maximum compressive stress (– 400 MPa).

During cycling, at the maximum tensile stress (400 MPa) for each cycle, a decreasing maximum intensity observed in the IPFs correlated well with decreasing macroscopic strain. This result was consistent with the correspondence between the variants selected and the macroscopic strains observed during strain-controlled, reverse, isothermal loading as presented in the previous section. More specifically, the martensite variant microstructure followed the macroscopic uniaxial strain and did not follow the compressive or tensile state of stress (within the limits investigated here) during stress-controlled, reverse, isothermal loading.

Constant Strain, Thermal Cycling

While isobaric and isothermal responses of shape memory NiTi have been extensively investigated, isostrain (thermal cycling under constant strain) loading has been limited to a few investigations [18, 20]. Thermal cycling at constant strain was investigated here and results are presented in the context of the isothermal loading results, presented in the previous section. Figure 7a shows the macroscopic stress–temperature response during thermal cycling between 40 and 165 °C under a constant strain of – 0.6 and 2%. The – 0.6 and 2% cases were performed in situ using synchrotron X-ray and neutron diffraction, respectively. For the first case, initial isothermal loading from zero to 2% tensile strain (from points 1 to 2) at room temperature corresponded to a macroscopic stress increase of 261 MPa. The specimen was held at constant strain of 2% (in strain control) and heated (from points 2 to 3) to a UCT = 165 °C corresponding to a blocking stress of 440 MPa. In order to ensure adequate statistics for the diffraction measurements, the specimen was held at the

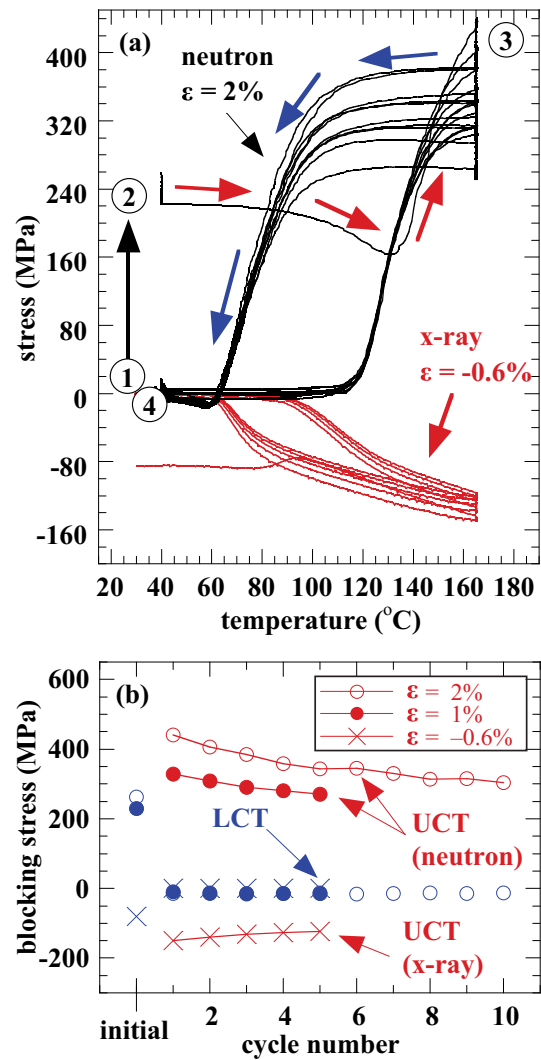


Fig. 7 Thermal cycling between 40 and 165 °C under constant strain for shape memory NiTi: **a** stress–temperature response with 2 and – 0.6% pre-strain performed at SMARTS and HEMS, respectively (indicated by “neutron” and “X-ray”, respectively, see text for details on the diffraction instruments used) and **b** blocking stress at the lower cycle temperature (LCT) and upper cycle temperature (UCT) with cycle number for all cases

UCT for 30 min during each cycle. During this hold time, a relaxation of stress occurred as observed in Fig. 7a. The specimen was then cooled (from points 3 to 4) to a LCT of 40 °C which resulted in the stress dropping to – 14.7 MPa, thus completing the first cycle. Figure 7b shows the blocking stress observed at the LCT and UCT for each cycle during ten thermal cycles under a constant strain of – 0.6, 1, and 2%, respectively.

Figure 8 shows the IPFs corresponding to thermal cycling between 40 and 165 °C under a constant strain of 1 and 2% at the UCT. For the 2% case, the initial IPF (not shown) at zero stress and strain at room temperature had a maximum intensity 1.87 corresponding to a self-accommodated microstructure. Upon initial isothermal loading

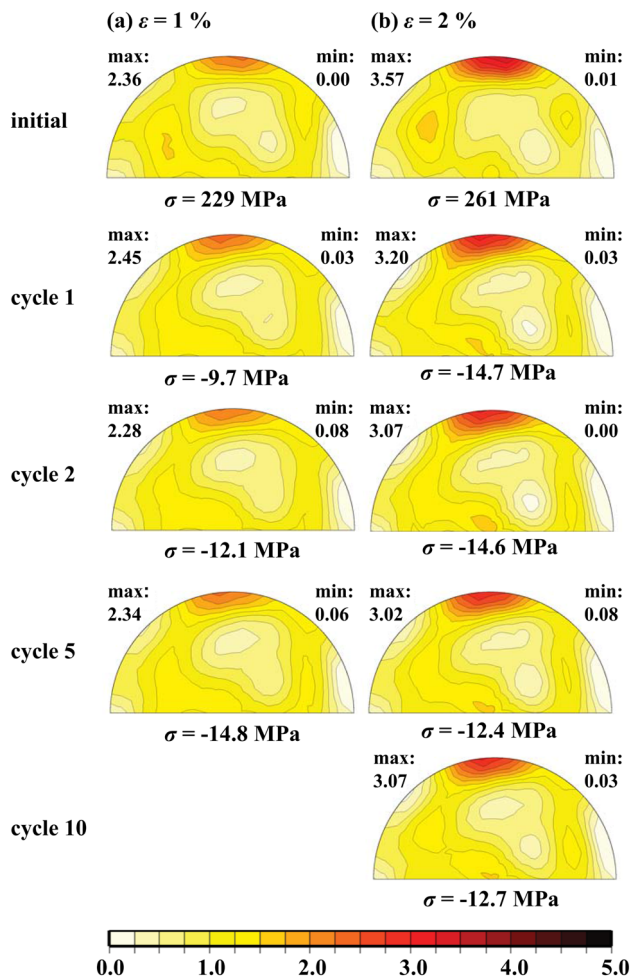


Fig. 8 Inverse pole figures (for the B19' phase at 40 °C) corresponding to diffracting planes perpendicular to the loading direction during thermal cycling (up to ten cycles) between 40 and 165 °C under a constant strain of **a** 1% and **b** 2%. For clarity presentation, the scale chosen is unique to this figure

(from points 1 to 2) to 2% strain, preferred variants are selected as indicated in the corresponding IPF by an increase in maximum intensity to 3.57 (compared to 3.21 observed at 2% tensile strain on initial loading in Fig. 2) near the 010 pole. Following the first heating and cooling cycle, this martensite variant microstructure was not significantly affected as indicated by a maximum intensity of 3.21 (near the 010 pole) observed in the corresponding IPF, despite a significant relaxation in stress (from 261 to – 14.1 MPa). This result demonstrates that the martensite variant microstructure formed by isothermal loading corresponded to a given strain and the correspondence was not affected by thermal cycling under constant strain, despite large changes in the macroscopic state of stress. The relaxation of stress and decrease in maximum intensity observed in the IPFs can be attributed to martensite variants accommodating the applied stress state during cooling. Overall, the response observed for thermal cycling at 1%

constant strain was comparable to the 2% constant strain case in terms of the correspondence between the martensite variant microstructure and the strain.

For the first thermal cycle, at a constant strain of 2%, a blocking stress of 440 MPa was observed at the UCT. During the next ten cycles, the blocking stress decreased with each cycle. While the rate of decrease reduced with each cycle, this behavior did not appear to stop for the number of cycles performed here. To explore possible mechanisms for the observed stress relaxation with cycling, the texture in B2 was investigated in IPFs. Figure 9 shows IPFs for B2 austenite taken at the UCT during thermal cycling (up to ten cycles) between 40 and 165 °C at a constant strain of 2%. For the first cycle, a maximum intensity of 1.67 was observed near the 110 pole in the corresponding IPF. The increased intensity near the 110 pole indicates a 110 fiber texture (assuming axial symmetry) in austenite. The texture observed here most likely

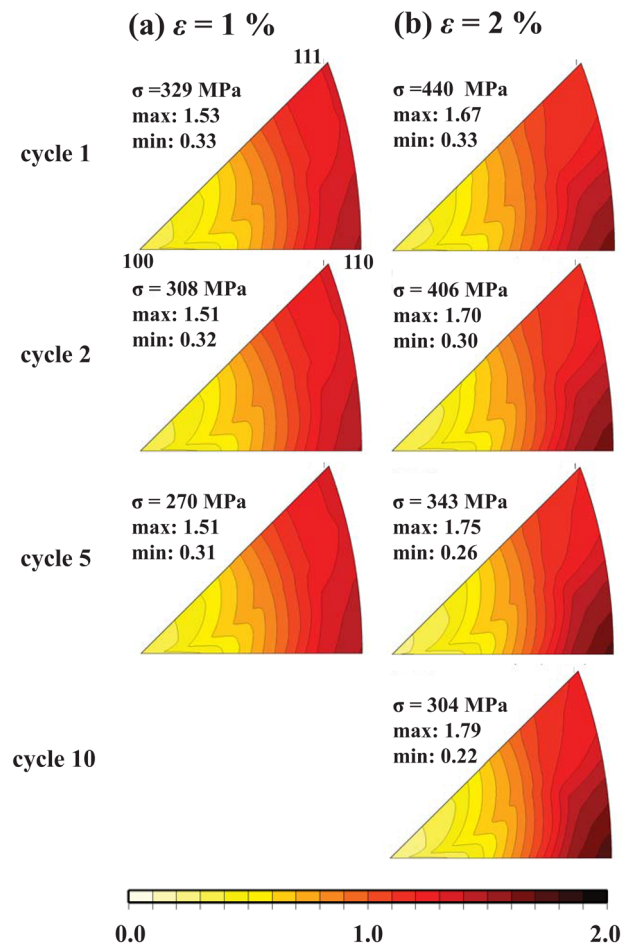


Fig. 9 Inverse pole figures (for the B2 phase at 165 °C) corresponding to diffracting planes perpendicular to the loading direction during thermal cycling (up to ten cycles) between 40 and 165 °C under a constant strain of **a** 1% and **b** 2%. For clarity presentation, the scale chosen is unique to this figure

developed during metallurgical processing and was considered to be weak. The maximum intensity observed in the IPFs on the first, second, fifth, and tenth cycles (with corresponding stress of 440, 406, 343, and 304 MPa, respectively) at the UCT was found to be 1.68, 1.70, 1.75, and 1.79, respectively. Therefore, over the ten thermal cycles under constant strain, the texture in B2 remained unchanged (within error), despite a significant decrease in macroscopic stress. The decrease in stress could still possibly be attributed to slip and deformation twinning which is not expected to produce a noticeable change in texture (for strains up to 10%) [35].

Thermal cycling at -0.6% constant strain using in situ synchrotron X-ray diffraction was also examined. A smaller strain was chosen here in order to reduce the contributions of variant and reorientation detwinning to the overall response and subsequently reveal other potential mechanisms. Additionally, synchrotron X-ray diffraction provided adequate diffraction statistics on the order of seconds as opposed to minutes compared to neutron diffraction thus eliminating possible time-dependent contributions, e.g., mechanisms contributing to stress relaxation observed at the UCT during neutron diffraction experiments.

Figure 10 shows synchrotron X-ray diffraction spectra from diffracting planes perpendicular to the loading direction (azimuthal angle, $\psi = 90^\circ$) at 165°C acquired during thermal cycling between 40 and 165°C under a constant strain of -0.6% for select B2 peaks. Also, shown are the spectra acquired from the second no-load thermal cycle, at the UCT. Note, no significant hold time at the UCT was required and therefore the stress did not discernibly relax. Results show a change in the lattice strain as seen from peak shifts between the no-load thermal cycle and subsequent thermal cycles. This was expected and can be attributed to elastic loading of B2 austenite under the blocking stress generated during thermal cycling under constant strain. From the first to fifth cycles, no significant changes in peak intensity and no peak broadening or peak shifts were observed, despite a decrease in the stress from -149.8 to -122.6 MPa over five thermal cycles (as shown in Fig. 7b).

Figure 11 shows the normalized intensities (I/I_0) of select B2 austenite peaks at 165°C as a function of azimuthal angle ψ (in 10° increments) during thermal cycling (up to five cycles) between 40 and 165°C under a constant strain of -0.6% . The 110 fiber texture can be observed as peaks in 110 intensity near azimuthal angles 90° and 270° , both of which angles correspond to the longitudinal direction in the specimen. No significant cycle-to-cycle change in intensity over the range of azimuthal angles was observed (for all crystallographic directions shown here) which indicates that no B2 austenite texture changes

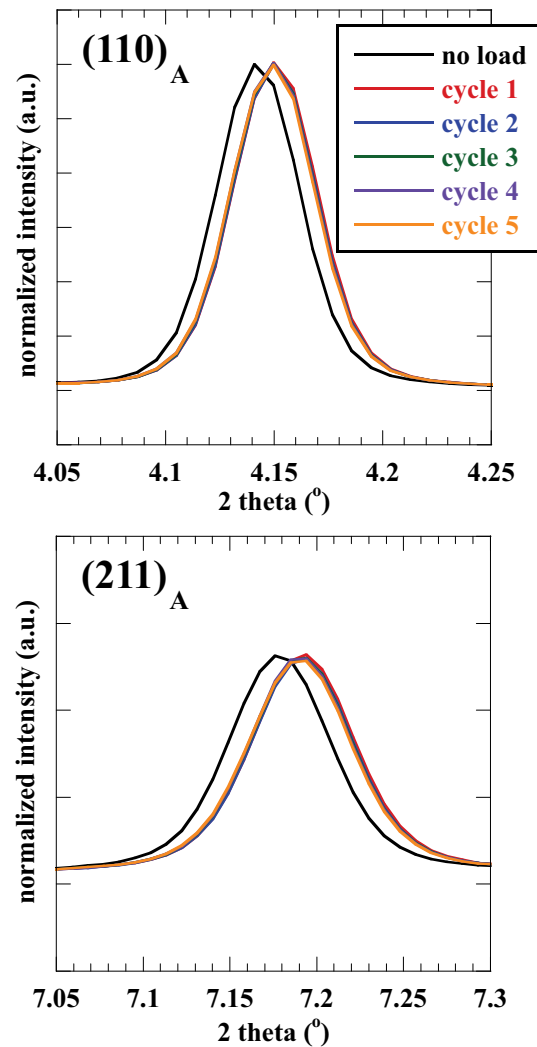


Fig. 10 In situ synchrotron X-ray diffraction spectra corresponding to diffracting planes perpendicular to the loading direction (azimuthal angle, $\psi = 90^\circ$) at 165°C during thermal cycling between 40 and 165°C under a constant strain of -0.6% for (110) and (211) B2 austenite peaks

occurred during cycling, despite a significant relaxation in the macroscopic blocking stress. Overall, no changes in texture or peak broadening were observed despite a significant relaxation in stress (at the UCT of each cycle) during constant strain thermal cycling. These results possibly point to slip and deformation twinning in B2 austenite, among other possible irrecoverable mechanisms, as was observed during isothermal loading and isobaric cycling of shape memory NiTi in Refs. [35, 36], respectively.

Texture Evolution and Crystallographic Theory

The purpose of this section is to discuss the results presented in previous sections, in the context of variant

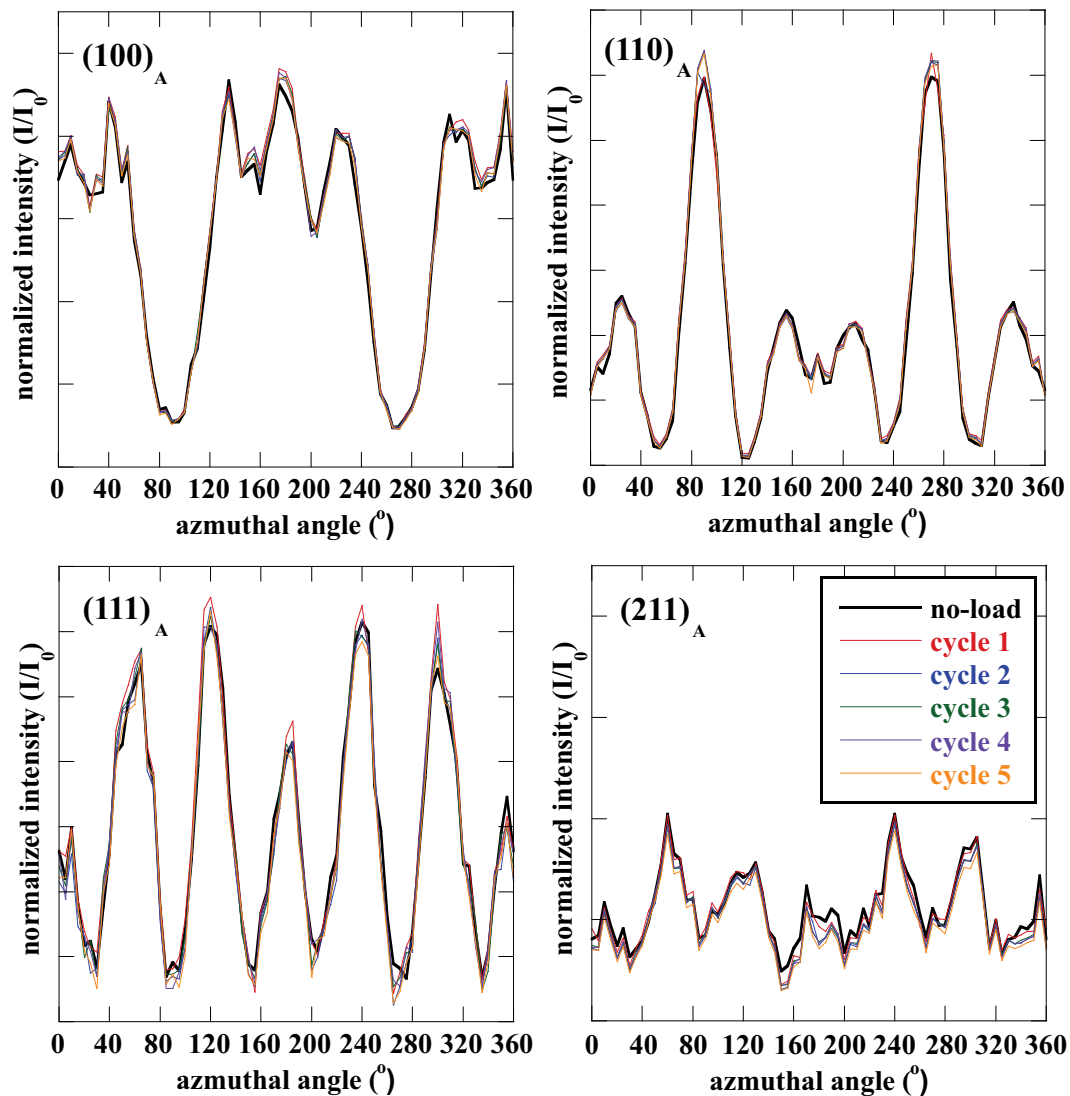


Fig. 11 Normalized intensities (I/I_0) of select B2 peaks at 165 °C as a function of azimuthal angle ψ (in 10° increments) during thermal cycling (up to five cycles) between 40 and 165 °C under a constant strain of -0.6%

reorientation and detwinning processes in martensitic NiTi and the fundamental thermoelastic nature of such processes. Towards this goal, comparisons are made between texture evolution observed during isothermal reverse loading and crystallographic theory. Bain strains between B2 austenite and B19' martensite structures were calculated (as done previously in Refs. [1, 37–39]) using lattice parameters obtained here by Rietveld refinement of neutron data by employing crystallographic theory for this alloy. The lattice parameters obtained by Rietveld refinement were $a = 2.91 \text{ \AA}$, $b = 4.65 \text{ \AA}$, $c = 4.13 \text{ \AA}$, and $\gamma = 97.75$ for monoclinic martensite and $d_{100,B2} = 3.03 \text{ \AA}$ for cubic austenite. The monoclinic angle is chosen to be between the minimum and maximum lattice vector lengths. Typically in other literature, b is chosen as the diad axis making β the monoclinic angle. To be consistent with the output of

the Rietveld refinements generated by GSAS and corresponding IPFs, c was chosen as the diad axis making γ the monoclinic angle. The transformation strains obtained here were mapped into an IPF in Fig. 12a to facilitate their discussion w.r.t. texture measurements observed through IPFs.

The maximum tensile ($\sim 11\%$ strain) and compressive ($\sim -7\%$ strain) transformation strains occur near the -120 and 210 poles, respectively. For convenience in the following discussion, Fig. 12b additionally shows representative IPFs (generated from lattice planes perpendicular to the loading direction) with the selected martensite variants under tension and compression (from Fig. 2). Reference [40] showed that martensite variant conversion occurs in a manner such that the correspondent variants, which produce the largest conversion strains, will grow at

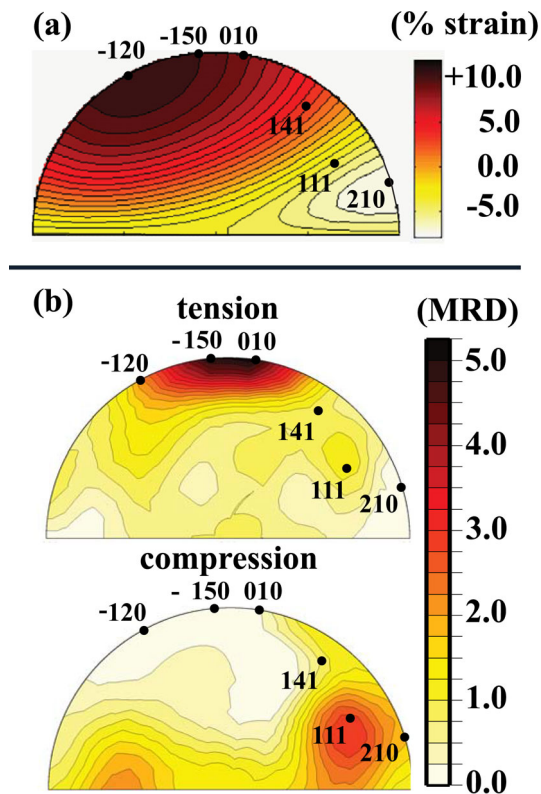


Fig. 12 **a** Bain strains calculated from crystallographic theory using lattice parameters obtained from Rietveld refinement of neutron data obtained in this work and **b** martensitic B19' NiTi inverse pole figures for tensile and compressive loading corresponding to lattice planes perpendicular to the loading direction. For clarity in presentation, the scale chosen in the inverse pole figures are unique to this figure

the expense of others in order to maximize macroscopic strain (under applied stress) in the polycrystalline aggregate. This was later noted and demonstrated for NiTi in Refs. [3, 38]. This can also be observed here in the IPFs presented in Fig. 12. Tensile loading causes an increase in pole density near the 010 direction (as shown in Fig. 12b) and the maximum variant conversion strain ($\sim 12\%$) was observed near the -120 direction (as shown in Fig. 12a). Likewise, compressive loading causes an increase in pole density near the 111 direction (as shown in Fig. 12b) and the maximum variant conversion strain ($\sim -7\%$) was observed near the 210 direction (as shown in Fig. 12a). The slight rotation between the observed preferred direction in the polycrystalline aggregate and that of the calculated maximum variant conversion strains can be attributed to intergranular interaction/constraints and the requirement to satisfy strain compatibility in the polycrystalline aggregate.

Figure 13 shows IPFs corresponding to diffracting planes with their plane normals at $\varphi = 46.3^\circ$ relative to the loading direction during the first cycle of isothermal, tensile followed by compressive, strain-controlled, reverse

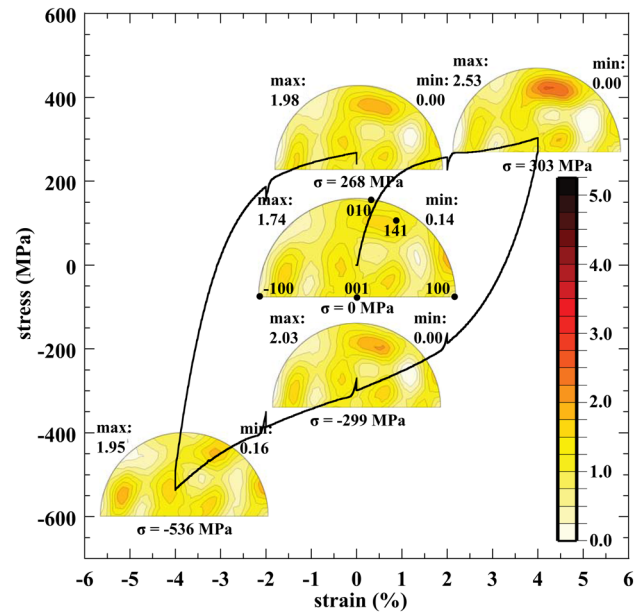


Fig. 13 Inverse pole figures corresponding to diffracting planes $\varphi = 46.3^\circ$ relative to the loading direction during the first cycle of isothermal tensile followed by compressive, strain-controlled, reverse loading of B19' martensitic NiTi at room temperature. Note, the IPFs presented here were generated from Rietveld refinements of diffraction spectra recorded by detector Bank 3 (as illustrated in Fig. 1). For clarity in presentation, the scale chosen in the inverse pole figures are unique to this figure

loading of B19' martensitic NiTi at room temperature. The IPFs presented here were generated from Rietveld refinements of diffraction spectra recorded by detector Bank 3 (as illustrated in Fig. 1). Tensile loading of the specimen to 4% strain resulted in an increase in intensity (to a maximum of 2.53) near the 141 pole, as observed in the corresponding IPF. This result is another example of the correlation between the variant microstructure and strain rather than stress, as martensite variants orient in a direction with low normal stresses to satisfy strain compatibility. Of significance is the placement of the detector (Fig. 1), data from which have previously not been reported for such experiments with NiTi at this neutron diffractometer. The magnitude of the strains near the 141 pole are intermediate (as opposed to maximum tension or compression), as seen in Fig. 12a. The evolving variant microstructure tracks the strain despite the anisotropy in strain in the sample, e.g., maximum tensile strain in the direction of uniaxial tensile loading and Poisson contraction in a direction 90 degrees to this direction and vice-a-versa. This variant microstructure evolution occurs in polycrystalline samples while satisfying stress and strain compatibility across variant boundaries.

The aforementioned behavior is also seen in ADPs wherein MRD (y-axis) of a specified crystallographic direction are represented over a range of specimen

directions (typically between the longitudinal loading and transverse directions). Figure 14a shows ADPs for the 010 direction corresponding to the first cycle of tension followed by compression, isothermal, reverse loading of B19' martensitic NiTi at room temperature. The ADPs presented here have three points of constraint, at $\varphi = 0^\circ$ (loading direction), 46.3° , and 90° (transverse direction) which correspond to detector banks 2, 3, and 1, respectively. The macroscopic response and IPFs corresponding to the loading direction ($\varphi = 0^\circ$) and the IPFs corresponding to ($\varphi = 46.3^\circ$) are shown in Figs. 2 and 13, respectively. In Fig. 14a, the variant microstructure manifests as increasing and decreasing intensities at $\varphi = 0^\circ$ and $\varphi = 90^\circ$, respectively, as the specimen was strained to 4% tensile strain. This indicates the 010 crystallographic direction

corresponds to variants that favor tensile deformation and the result is consistent with those observed in the IPFs in Fig. 2. At 4% tensile strain, the decreased intensity at $\varphi = 90^\circ$ is caused by a reduction due to Poisson's ratio in the transverse direction. Upon load reversal (from 4 to -4% strain), variants that favor tensile deformation reorient to variants which favor compressive deformation as indicated by decreased and increased intensities at $\varphi = 0^\circ$ and $\varphi = 90^\circ$, respectively. Figure 14b shows the ADP for the 111 direction which corresponds to variants which favor compressive deformation (as seen previously in Fig. 2). During this reverse loading (from 4 to -4% strain), variants which favor compressive deformation grew at the expense of variants which favor tensile deformation, as indicated by increased and decreased intensities at $\varphi = 0^\circ$ and $\varphi = 90^\circ$, respectively. Upon the second load reversal (returning to 0 from -4% strain), the variant microstructure returned to a near self-accommodated state as indicated by good agreement between 0% initial and 0% final strain, in both Fig. 14a, b. Also note that in both ADPs, corresponding to the 010 and 111 crystallographic directions, negligible changes were observed near $\varphi = 46.3^\circ$. Overall, results observed through the ADPs provided additional evidence that variants, which maximize strain, are preferentially selecting to the direction of applied stress at the expense of variants that are less favorable (or those which produce less strain) in the polycrystalline aggregate.

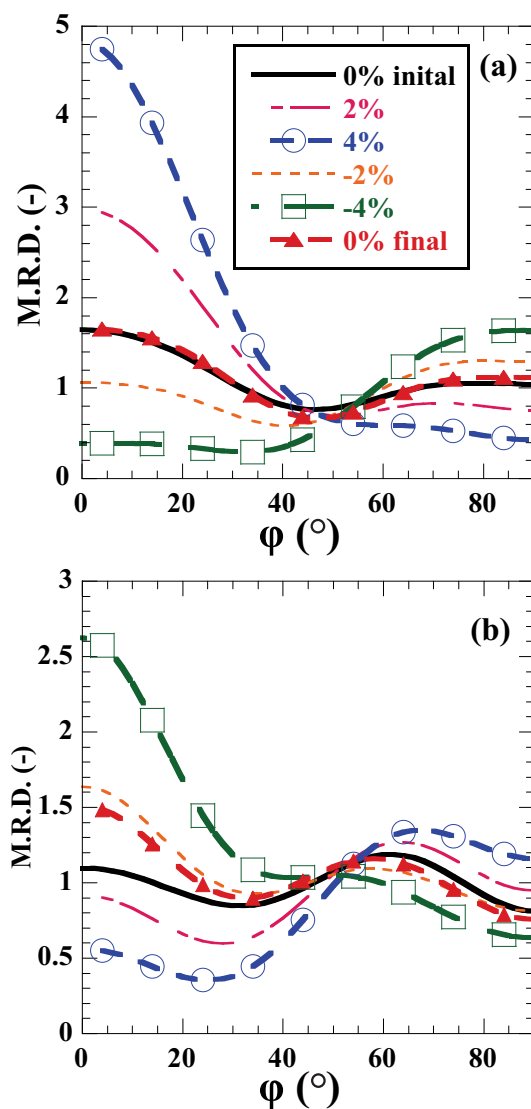


Fig. 14 Axial distribution plots corresponding to the first cycle of tension followed by compression, isothermal, reverse loading of B19' martensitic NiTi at room temperature: **a** 010 and **b** 111

Conclusions

Loading path and control mode effects in polycrystalline shape memory NiTi was investigated by recourse to in situ neutron and synchrotron X-ray diffraction performed during reverse mechanical loading and constant strain thermal cycling. In situ neutron and synchrotron X-ray diffraction provided information representative of the bulk, i.e., phase fraction and texture evolution that was tracked during stress- and strain-controlled, isothermal, reverse loading and constant strain thermally cycling of shape memory polycrystalline NiTi. Results were discussed in the context of fundamental thermoelastic mechanisms in NiTi and the following conclusions were made.

1. Reverse isothermal loading of martensite demonstrated that the martensite variant microstructure correlated directly with the macroscopic uniaxial strain and did not correlate with the compressive or tensile state of stress. Additionally, the isothermal reversibility of texture and its correspondence with a given macroscopic strain was demonstrated when loading was reversed and the strain returned to zero. This

conclusion was first realized in Ref. [6] and was demonstrated again here as the foundation for the following conclusions. Of significance in this work is the placement of the third detector, data from which have previously not been reported for such experiments with NiTi.

2. The evolving texture was independent of the initial loading direction (i.e., the results obtained were similar for both, compression–tension and tension–compression, reverse loading paths). While this can be expected due to the reversible thermoelastic nature of deformation in NiTi, this observation despite the tension–compression asymmetry in irreversible processes (seen in this work as remnant or residual texture) is noteworthy and speaks to the ability of martensite variants to accommodate these irreversible deformation processes.
3. During cyclic stress- and strain-controlled, reverse, isothermal, load cycling, a change of slope of the stress–strain response was observed as maximum strain values decreased and stress values increased, with each cycle, in respective control modes. The texture tracked the strain despite this evolution of the overall macroscopic stress–strain response again due to the ability of martensite variants to accommodate deformation processes associated with cyclic loading in either stress- or strain-control modes.
4. During thermal cycling under constant strain (up to 2% tensile), the maximum stress values decreased to zero at the LCT and gradually decreased with each cycle at the UCT. Despite relaxation of stress in both martensite and austenite, the evolving texture again directly tracked the strain during constant strain thermal cycling. Additionally, no major microstructural changes (specifically, of texture) were observed in the B2 phase during cycling. This observation can be reconciled with the direct correspondence that exists between the austenite B2 and martensite B19' phases and the ability of the variant microstructure to accommodate any irreversible mechanism responsible for the stress relaxation.

The preceding conclusions point to multiple loading paths (which includes one or more of isobaric, isothermal, or isostrain loading paths [6, 36]) over multiple cycles under stress- or strain-control resulting in equivalent variant microstructures that directly correlate with the macroscopic strain. Thus, a training regimen that reduces the number of training cycles in stress–strain–temperature space in order to obtain the desired variant microstructure has implications for increasing the engineering life of NiTi components.

Acknowledgements The authors would like to acknowledge funding from the NASA Fundamental Aeronautics Program., Supersonics Project (Grant No. NNX08AB51A) and Subsonic Fixed Wing Project (Grant No. NNX11AI57A). This work has benefited from the use of the Lujan Neutron Scattering Center at LANSCE, which was funded by the Office of Basic Energy Sciences (DOE). LANL is operated by Los Alamos National Security LLC under DOE under Contract No. DE-AC52-06NA25396. This work also benefited from the use of the HEMS beamline at the German high-brilliance synchrotron radiation storage ring PETRA III at DESY. The authors thank T. Sisneros and D.W. Brown at LANL and N. Schell at DESY for technical support.

References

1. Bhattacharya K (ed) (2003) *Microstructure of martensite: why it forms and how it gives rise to the shape-memory effect?*. Oxford University Press, New York
2. Miyazaki S, Otsuka K, Wayman CM (1989) The shape memory mechanism associated with the martensitic transformation in TiNi alloys—I. Self-accommodation. *Acta Metall* 37(7):1873–1884
3. Otsuka K, Ren X (2005) Physical metallurgy of Ti-Ni-based shape memory alloys. *Prog Mater Sci* 50(5):511–678
4. Yamauchi K, Ohkata I, Tsuchiya K, Miyazaki S (eds) (2011) *Shape memory and superelastic alloys: technologies and applications*. Woodhead Publishing, Oxford
5. Saleeb AF, Padula SA II, Kumar A (2011) A multi-axial, multi-mechanism based constitutive model for the comprehensive representation of the evolutionary response of SMAs under general thermomechanical loading conditions. *Int J Plast* 27(5):655–687
6. Nicholson DE, Padula SA II, Benafan O, Vaidyanathan R (2017) Texture evolution during isothermal, isostrain and isobaric loading of polycrystalline shape memory NiTi. *Appl Phys Lett* 110(25):251903
7. Nicholson DE, Bass MA, Mabe JH, Benafan O, Padula SA, Vaidyanathan R (2016) Heating and loading paths to optimize the performance of trained shape memory alloy torsional actuators. ASME (2016), conference on smart materials, adaptive structures and intelligent systems. American Society of Mechanical Engineers, New York
8. Benafan O, Padula SA II, Noebe RD, Sisneros T, Vaidyanathan R (2012) Role of B19' martensite deformation on the stability of NiTi two-way shape memory effect. *J Appl Phys* 112(9):093510
9. Stebner AP, Vogel SC, Noebe RD, Sisneros T, Clausen B, Brown DW, Garg A, Brinson LC (2013) Micromechanical quantification of elastic, twinning, and slip strain partitioning exhibited by polycrystalline, monoclinic nickel-titanium during large uniaxial deformations measured via in situ neutron diffraction. *J Mech Phys Solids* 61(11):2302–2330
10. Wagner MFX, Windl W (2008) Lattice stability, elastic constants and macroscopic moduli of NiTi martensites from first principles. *Acta Mater* 56(20):6232–6245
11. Qiu S, Clausen B, Padula SA II, Noebe RD, Vaidyanathan R (2011) On elastic moduli and elastic anisotropy in polycrystalline martensitic NiTi. *Acta Mater* 59(13):5055–5066
12. Stebner AP, Brown DW, Brinson LC (2013) Young's modulus evolution and texture-based elastic–inelastic strain partitioning during large uniaxial deformations of monoclinic nickel–titanium. *Acta Mater* 61(6):1944–1966
13. Ezaz T, Sehitoglu H, Maier HJ (2011) Energetics of twinning in martensitic NiTi. *Acta Mater* 59(15):5893–5904
14. Xie ZL, Liu Y (2004) HRTEM study of $\langle 011 \rangle$ type II twin in NiTi shape memory alloy. *Philos Mag* 84(32):3497–3507

15. Xie ZL, Liu Y, Van Humbeeck J (1998) Microstructure of NiTi shape memory alloy due to tension–compression cyclic deformation. *Acta Mater* 46(6):1989–2000
16. Liu Y, Xie Z, Van Humbeeck J (1999) Cyclic deformation of NiTi shape memory alloys. *Mater Sci Eng A* 273–275(15):673–678
17. Nishida M, Ii S, Kitamura K, Furukawa T, Chiba A, Hara T, Hiraga K (1998) New deformation twinning mode of B19' martensite in Ti-Ni shape memory alloy. *Scr Mater* 39(12):1749–1754
18. Benafan O, Noebe RD, Halsmer TJ, Padula SA II, Bigelow GS, Gaydos DJ, Garg A (2016) Constant-strain thermal cycling of a Ni_{50.3}Ti_{29.7}Hf₂₀ high-temperature shape memory alloy. *Shape Mem Superelasticity* 2(2):1–10
19. Benafan O, Noebe RD, Halsmer TJ (2016) Static rock splitters based on high temperature shape memory alloys for planetary explorations. *Acta Astronaut* 118:137–157
20. Benafan O, Padula SA II, Noebe RD, Brown DW, Clausen B, Vaidyanathan R (2013) An in situ neutron diffraction study of shape setting NiTi shape memory alloy. *Acta Mater* 61(10):3585
21. Qiu S, Krishnan VB, Padula SA, Noebe RD, Brown DW, Clausen B, Vaidyanathan R (2009) Measurement of the lattice plane strain and phase fraction evolution during heating and cooling in shape memory NiTi. *Appl Phys Lett* 95(14):141906
22. Padula SA, Qiu S, Gaydos D, Noebe R, Bigelow G, Garg A, Vaidyanathan R (2012) Effect of upper-cycle temperature on the load-biased, strain-temperature response of NiTi. *Metall Mater Trans A* 43:4610–4621
23. Manchiraju S, Gaydos D, Benafan O, Noebe R, Vaidyanathan R, Anderson PM (2011) Thermal cycling and isothermal deformation response of polycrystalline NiTi: simulations vs. experiment. *Acta Mater* 59(13):5238–5249
24. Bourke MAM, Dunand DC, Ustundag E (2002) SMARTS—a spectrometer for strain measurement in engineering materials. *Appl Phys Lett* 74:S1707
25. Von Dreele RB, Jorgensen JD, Windsor CG (1982) Rietveld refinement with spallation neutron powder diffraction data. *J Appl Crystallogr* 15:581–589
26. Larson AC, Von Dreele RB (2004) General Structure Analysis System (GSAS). Report LAUR 86-748. Los Alamos National Laboratory, New Mexico
27. Krishnan V, Manjeri RM, Clausen B, Brown D, Vaidyanathan R (2008) Analysis of neutron diffraction spectra acquired in situ during mechanical loading of shape memory NiTiFe at low temperatures. *Mater Sci Eng A* 481:3–10
28. Vaidyanathan R, Bourke MAM, Dunand DC (1999) Analysis of neutron diffraction spectra acquired in situ during stress-induced transformations in superelastic NiTi. *J Appl Phys* 86(6):3020–3029
29. Von Dreele RB (1997) Quantitative texture analysis by Rietveld refinement. *J Appl Crystallogr* 30:517–525
30. Wessel P, Smith WHF (1995) New version of the generic mapping tools. *EOS Trans Am Geophys Union* 76(33):329
31. Benafan O, Garg A, Noebe RD, Bigelow GS, Padula SA, Gaydos DJ, Schell N, Mabe JH, Vaidyanathan R (2014) Mechanical and functional behavior of a Ni-rich Ni 50.3 Ti 29.7 Hf 20 high temperature shape memory alloy. *Intermetallics* 50:94–107
32. Benafan O, Garg A, Noebe RD, Skorpenske HD, An K, Schell N (2017) Deformation characteristics of the intermetallic alloy 60NiTi. *Intermetallics* 82:40–52
33. Vaidyanathan R, Bourke MAM, Dunand DC (2001) Texture, strain, and phase-fraction measurements during mechanical cycling in superelastic NiTi. *Metall Mater Trans A* 32(13):777–786
34. Rathod CR, Clausen B, Bourke MAM, Vaidyanathan R (2006) Neutron diffraction investigation of hysteresis reduction and increase in linearity in the stress-strain response of superelastic NiTi. *Appl Phys Lett* 88(20):201919
35. Benafan O, Noebe RD, Padula SA II, Garg A, Clausen B, Vogel S, Vaidyanathan R (2013) Temperature dependent deformation of B2 austenite in a NiTi shape memory alloy. *Int J Plast* 51:103–121
36. Benafan O, Noebe RD, Padula SA II, Brown DW, Vogel S, Vaidyanathan R (2014) Thermomechanical cycling of a NiTi shape memory alloy-macroscopic response and microstructural evolution. *Int J Plast* 56:99–118
37. Otsuka K, Wayman CM (eds) (1999) *Shape memory materials*. Cambridge University Press, Cambridge
38. Ye B, Majumdar BS, Dutta I (2009) Texture development and strain hysteresis in a NiTi shape-memory alloy during thermal cycling under load. *Acta Mater* 57(8):2403–2417
39. Ye B, Majumdar BS, Dutta I (2007) Texture memory and strain-texture mapping in a NiTi shape memory alloy. *Appl Phys Lett* 91(6):061918
40. Saburi T, Nenno S (1981) *Solid phase transformations*. TMS-AIME, Warrendale